Available online at www.sciencedirect.com

ScienceDirect

Acta Materialia 59 (2011) 5238–5249

Acta MATERIALIA

www.elsevier.com/locate/actamat

Thermal cycling and isothermal deformation response of polycrystalline NiTi: Simulations vs. experiment

Sivom Manchiraju [a], Darrell Gaydosh [b], Othmane Benafan [c], Ronald Noebe [b], Raj Vaidyanathan [c], Peter M. Anderson [a,*]

[a] *Materials Science and Engineering, The Ohio State University, Columbus, OH 43210, USA*
[b] *NASA Glenn Research Center, 21000 Brookpark Rd., Cleveland, OH 44135, USA*
[c] *Mechanical, Materials, and Aerospace Engineering, University of Central Florida, 4000 Central Florida Blvd., Orlando, FL 32816, USA*

Received 1 April 2011; received in revised form 27 April 2011; accepted 28 April 2011
Available online 3 June 2011

Abstract

A recent microstructure-based FEM model that couples crystal-based plasticity, the B2 ↔ B19′ phase transformation and anisotropic elasticity at the grain scale is calibrated to recent data for polycrystalline NiTi (49.9 at.% Ni). Inputs include anisotropic elastic properties, texture and differential scanning calorimetry data, as well as a subset of recent isothermal deformation and load-biased thermal cycling data. The model is assessed against additional experimental data. Several experimental trends are captured – in particular, the transformation strain during thermal cycling monotonically increases and reaches a peak with increasing bias stress. This is achieved, in part, by modifying the martensite hardening matrix proposed by Patoor et al. [Patoor E, Eberhardt A, Berveiller M. J Phys IV 1996;6:277]. Some experimental trends are underestimated – in particular, the ratcheting of macrostrain during thermal cycling. This may reflect a model limitation that transformation–plasticity coupling is captured on a coarse (grain) scale but not on a fine (martensitic plate) scale.
Published by Elsevier Ltd. on behalf of Acta Materialia Inc.

Keywords: Shape memory alloys; Thermal cycling; Finite element

1. Introduction

An important challenge to shape memory alloy (SMA) models is to capture the actuation response [1–3]. A representative situation is shown in Fig. 1a, where the material is subjected to a constant tensile bias stress Σ_{bias} Upon heating, the SMA contracts by a macroscopic transformation strain E_T (feature F7). Other important features are the hysteretic width $\Delta\theta_H$ (feature F6), widths $\Delta\theta_{A-M}$ (feature F8) and $\Delta\theta_{M-A}$ for the austenite-to-martensite and martensite-to-austenite transformations, respectively, and the open loop strain per thermal cycle, ΔE_{cycle} These quantities typically depend on Σ_{bias}, composition, processing history and microstructural features such as single/polycrystalline orientation/texture, precipitate morphology, dislocation substructure and internal stress (e.g. [4]).

SMA models can be characterized by their microstructural detail and phenomenological nature. For example, some track the volume fractions of stress-induced vs. thermally induced martensite via state variables [5,6] or adopt a functional dependence of transformation strain on the total martensite volume fraction and stress [7]. Others include a phenomenological description of transformation-induced plasticity [8–11]. Variant-level models (e.g. [12–20]) track the volume fraction of individual martensite variants, thereby capturing effects of texture and crystal orientation. One version includes a recursive algorithm method that adjusts interactions between competing tetradomains in order to reproduce neutron diffraction data [21]. The method captures the evolution of martensite volume fraction and local stress for various $\langle hkl \rangle$ sets of domains [22].

* Corresponding author. Tel.: +1 614 292 1537.
E-mail address: anderson.1@osu.edu (P.M. Anderson).

1359-6454/$36.00 Published by Elsevier Ltd. on behalf of Acta Materialia Inc.
doi:10.1016/j.actamat.2011.04.063

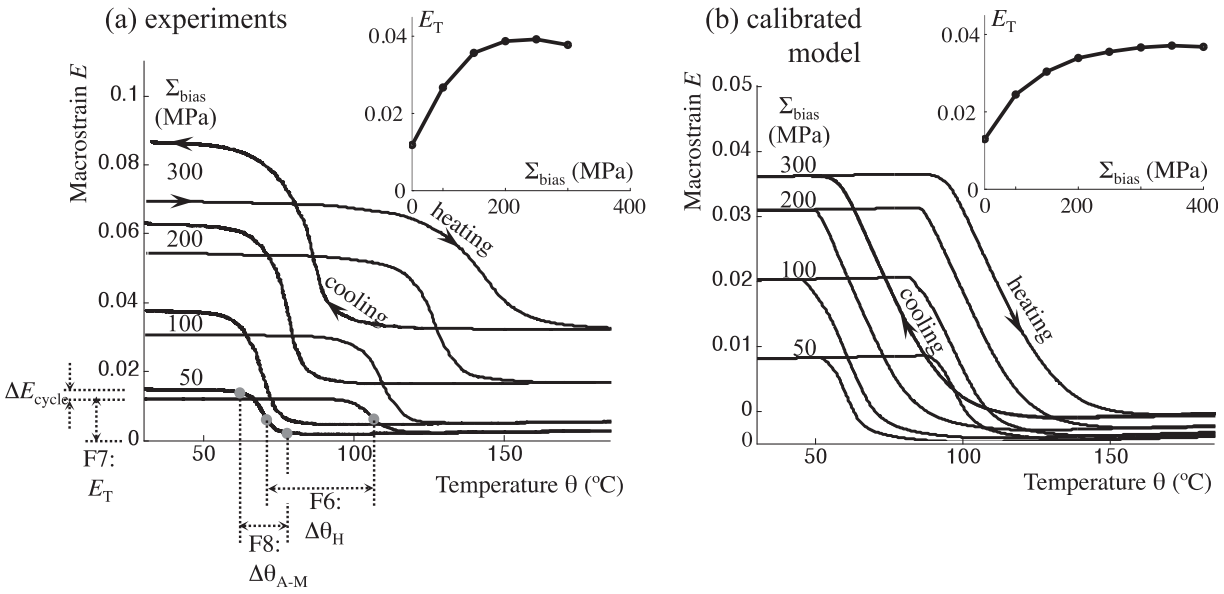

Fig. 1. Axial macrostrain E vs. temperature θ during thermal cycling with an axial bias stress Σ_{bias}: (a) experimental data for the 49.9 at.% Ni–Ti alloy and (b) calibrated model results. The inserts show the transformation strain E_T vs. Σ_{bias}, where E_T is defined by feature **F7** in (a). The calibrated model parameters are presented in Table 1.

A particular challenge to simulate actuator performance is to capture the initial, gradual increase in E_T with Σ_{bias}, the attainment of a peak E_T at moderate Σ_{bias} and the decrease in E_T at larger Σ_{bias} (Fig. 1a, inset). The gradual increase in E_T tests model assumptions about martensite interactions. These can be formulated between individual twinned habit plane variants (hpv) [14–17,23], hpv groups [24] and lattice correspondence variants (lcv) [25], or groups thereof [21,22]. An implementation of the first type by Patoor et al. [23] has been used (e.g. [15–17]), but the predicted E_T increases too abruptly with Σ_{bias} [25].

The peak in E_T with Σ_{bias} tests model assumptions concerning plasticity. Most do not incorporate it at all [12–16], including the aforementioned recursive model [21,22]. Some recent efforts have included martensite plasticity, either in J2-based [18,26] or crystal-based [17] forms. However, austenite rather than martensite plasticity has been observed in recent transmission electron microscope studies of pseudoelastically deformed, solutionized 50.7 at.% Ni–Ti single crystal pillars [27] and cold-worked 50.8 at.% Ni–Ti wires [28], as well as thermally cycled, single-crystal 50.4 at.% Ni–Ti [29]. In particular, a detailed analysis reveals that transformation-induced dislocations have Burgers vectors and slip planes with rationale directions in the austenite basis rather than the martensite basis [27]. These observations follow earlier work documenting the formation of planar dislocation arrays during load-biased thermal cycling of 50.1 and 50.4 at.% Ni–Ti [30]. Plastic deformation has also been proposed to explain progressive widening of the {1 1 0} B2 peak during load-biased thermal cycling [31].

Consequently, a principal contribution of this paper is to determine whether a crystal-based modeling approach that incorporates austenite plasticity can capture the key thermal cycling features shown in Fig. 1a as well as other data. This recent finite element (FE) approach [32] couples a crystal-based description of the evolution of martensite hpv by Thamburaja and Anand [13] with a crystal-based description of austenite plasticity based on Peirce et al. [33]. Thus, it is able to assess the Patoor et al. [23] formalism for hpv–hpv interaction as well as hpv–crystal plasticity interaction. Other unique features are inclusion of rigorous formalisms for anisotropic elastic deformation in the austenite and martensite phases, as well as predictions of the orientation of individual Bain strain variants of martensite. Recently reported elastic constants for monoclinic martensite [34] are included, as well as the appropriate invariant-plane condition between austenite and martensite – a feature not satisfied in a recent self-consistent approach to incorporate anisotropic elasticity [35].

The structure of the manuscript is as follows: Section 2 describes experimental data for the polycrystalline 49.9 at.% Ni–Ti material system, performed in support of the modeling activity. Section 3 describes the FE model. Section 4 presents the process for calibrating the model parameters to a subset of experimental data, and Section 5 assesses predictions of the calibrated model to additional data. Section 6 provides an overall assessment of model capabilities and conclusions.

2. Experimental characterization

2.1. Material system and history

The binary 49.9 at.% (55 wt.%) Ni–Ti alloy used in this study is described elsewhere [2]. It was produced by Special

Metals, New Hartford, NY and supplied as 10 mm diameter rods in a hot-rolled/hot-drawn and hot-straightened condition. The specific thermo-mechanical processing history is proprietary. The alloy is single phase, with a dynamically recrystallized and equiaxed grain structure with ~40 μm average grain size.

All experimental measurements on as-machined specimens were preceded by two no-load thermal cycles from 30 to 200 °C at 20 °C min^{-1}. The nominal purpose is to reduce internal stress generated by material processing and machining.

2.2. Texture analysis

The as-received alloy had a very weak recrystallization texture. Fig. 2a shows the pole figures in the austenite phase at 200 °C. They were obtained using the high-pressure preferred orientation (HIPPO) neutron diffractometer at Los Alamos National Laboratory (LANL) [36].

2.3. Differential scanning calorimetry

Differential scanning calorimetry (DSC) tests were performed to measure the heat of transformation, Q_{DSC}, the martensite start and finish temperatures, θ_{MS} and θ_{MF}, and the austenite start and finish temperatures, θ_{AS} and θ_{AF} [2]. Key results were determined from a $n = 7$ DSC sampling size and are summarized in Section 4.2.

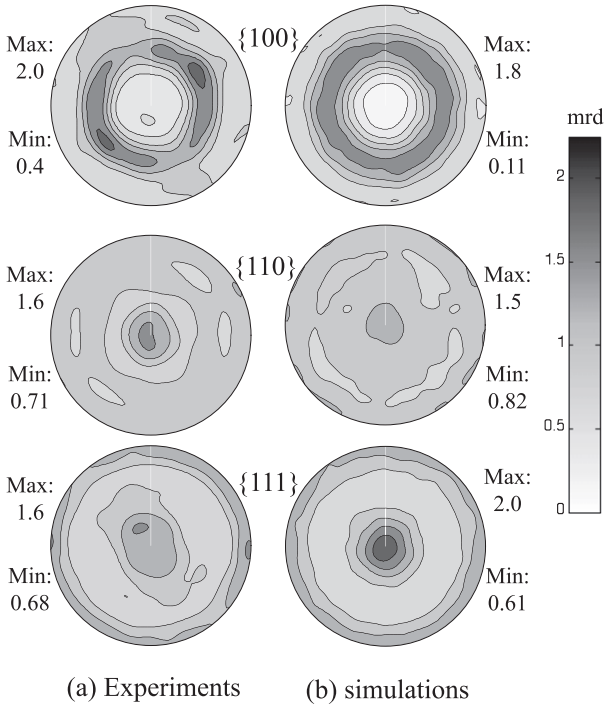

Fig. 2. Pole figures for as-received austenitic polycrystalline 49.9 at.% Ni–Ti at 200 °C from (a) neutron diffraction data using HIPPO and (b) simulations based on SMARTS diffraction data [2] for the same material at 200 °C, using POPLA software [46] and assuming axisymmetry. A stronger (1 1 1) and weaker (1 0 0) texture are apparent.

2.4. Pseudoelastic and plastic strains above θ_{AF}

Fig. 3a shows the uniaxial tension stress–strain response at $\theta_0 = 130$ °C for maximum imposed axial strains $E_{max} = 0.02$ and 0.04, and also at 215 °C for $E_{max} = 0.04$. Stress-induced martensite forms during deformation above θ_{AF} and some is retained upon unloading. A small axial strain rate of 10^{-4} s^{-1} was used to help ensure isothermal conditions. After E_{max} was attained, the sample was unloaded isothermally and then heated to 600 °C under no load. During heating, the macrostrain E decreased due to recovery (transformation) of stabilized martensite to austenite. It was then cooled back to θ_0 Recovery was confirmed by noting that the macrostrain–temperature (E–θ) response during initial cooling is consistent with the thermal expansion coefficient of austenite [37]. The strain $E_{post\text{-}heat}$ (feature F13, Fig. 3a) at θ_0 is expected to be due primarily to plastic deformation.

This NiTi alloy does not exhibit a strong, "flag-like" pseudoelastic response, as typically observed above θ_{AF} in Ni-rich NiTi alloys [12–15,28,29,38–42] or cold-worked and annealed Ti-rich NiTi alloys [43]. The more idealized pseudoelastic response, with clear loading and unloading plateaus and large recoverable strains, is obtained in microstructures that suppress plastic deformation [44] yet permit stress-induced transformation. In practice, this is achieved through grain refinement [28,42], cold work with partial recovery [43] or precipitation strengthening of Ni-rich NiTi alloys through suitable heat treatment [38–41]. Such strategies were not pursued here since the goal was to study the simultaneous effects of plasticity and transformation. Indeed, the features in Fig. 3a (and Fig. 1a) show evidence of both plasticity and pseudoelastic transformation, making it a suitable system to test the polycrystalline simulations.

2.5. Load-biased thermal cycling

Fig. 1a shows the E–θ response of the NiTi alloy at different values of uniaxial bias stress (Σ_{bias}). The stress level was achieved by imposing a 10^{-4} s^{-1} axial strain rate at $\theta_{min} = 30$ °C, where martensite is stable, until the desired stress was reached at constant temperature. The controller was switched into load control and the stress was held constant. This was followed by thermal cycling up to $\theta_{max} = 200$ °C and back to $\theta_{min} = 30$ °C at constant Σ_{bias} The second thermal cycle responses are shown in Fig. 1a, as well as the transformation strain E_T vs. Σ_{bias} (inset).

2.6. In situ neutron diffraction

Neutron diffraction spectra were obtained during stress-biased thermal cycling, using the protocol in Section 2.5. These measurements were obtained in "time-of-flight" mode using the Spectrometer for MAterials Research at Temperature and Stress (SMARTS) facility at LANL.

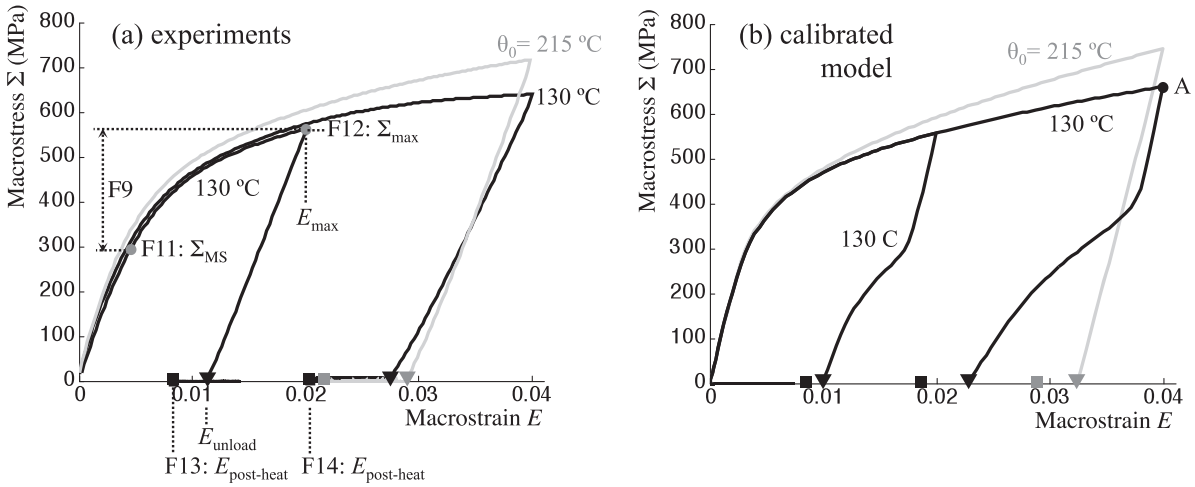

Fig. 3. Axial macrostress Σ vs. macrostrain E at $\theta_0 = 130$ vs. 215 °C showing (a) experimental data for the 49.9 at.% Ni–Ti alloy and (b) calibrated model results. E_{unload} and $E_{\text{post-heat}}$ are the respective macrostrains after unloading and after a subsequent 600 °C heat treatment of the unloaded sample. The calibrated model parameters are presented in Table 1.

Two detector banks furnished the diffracted intensity vs. d-spacing from two groups of crystallographic planes: those parallel and those perpendicular to the loading axis. The data give the evolution of martensite and austenite (volume fraction and orientation) during thermal cycling. Additional details are provided in Ref. [2] and the references therein.

3. Polycrystalline simulations and constitutive relation

3.1. Polycrystalline simulations

A brief description of the finite element representation of the polycrystal and boundary conditions is provided, with emphasis on texture specification and new model extensions as noted in Section 1. Additional details are provided in Ref. [32].

3.1.1. Discretization at the grain scale and texture specification

The polycrystal was modeled by a $7 \times 7 \times 7$ cube assembly of 8-node three-dimensional brick elements (C3D8 for isothermal analyses and C3D8T for thermo-mechanical analyses) using the commercial FE software ABAQUS [45]. Each element represented a grain with an assigned crystal orientation of the austenite (B2) phase. These orientations were based on a simulated texture for the as-received NiTi (Fig. 2b), obtained by processing SMARTS data [2] with the texture analysis software POPLA [46], assuming an axisymmetric texture. This assumption and the stronger (1 1 1) and relatively weaker (1 0 0) textures present in the SMARTS data compare favorably with subsequent HIPPO data shown in Fig. 2a (Section 2.2). The number of grains, $N_{\text{grain}} = 343$, in the simulations is sufficient since the macroscopic response does not change significantly for $N_{\text{grain}} > 343$.

3.1.2. Predeformation $E_{p(pre)}$ in the austenitic state

Some internal stress is expected in the samples prior to testing, even though the material was hot-worked and two no-load or stress-free thermal cycles were imposed before testing. The simulations introduced internal stress via predeformation in the austenitic state. This was achieved by heating to 300 °C, at which temperature austenite is stable, imposing a macroscopic plastic prestrain $E_{\text{p(pre)}}$ at $10^{-4}\,\text{s}^{-1}$, unloading, then cooling to the desired test temperature θ_0 $E_{\text{p(pre)}}$ was varied to match the experimental data (Section 4.3).

3.1.3. Isothermal deformation testing and post-heating

The polycrystal was strained to $E_{\max}$ at some constant temperature $\theta_0 > \theta_{\text{AF}}$ and then unloaded. This was achieved via prescribed normal displacement rates and zero shear tractions on the top and bottom surfaces, equivalent to an axial strain rate of $\pm 10^{-4}\,\text{s}^{-1}$. The transverse faces were traction free. The macrostrain E_{unload} after unloading was partitioned into plastic and transformation contributions by integration of the local plastic and transformation strains over the polycrystal. The simulations assumed spatially uniform, isothermal conditions. This is considered reasonable since the small imposed strain rate minimizes local heating and heat transfer rates associated with the austenite–martensite phase transformation. Fig. 3b shows results using the calibrated model.

3.1.4. Stress-biased thermal cycling

The polycrystal was heated to the maximum cycling temperature $\theta_{\max} = 190$ °C, then the bias stress Σ_{bias} was imposed using an axial strain rate of $10^{-4}\,\text{s}^{-1}$. The sample was then cycled between $\theta_{\min} = 30$ °C and $\theta_{\max}$ at ± 0.08 °C s^{-1}. The simulations assumed a spatially uniform temperature, which is reasonable, given the small heating/cooling rate. The simulations began the load application

and cycling at θ_{max}, compared to θ_{min} for the experiments. However, previous experiments [3] and the current results show this does not affect key parameters such as transformation strain. Fig. 1b shows results using the calibrated model.

3.1.5. In situ neutron diffraction simulations

Three post-processing steps were performed to compare simulations and experiments. First, the predicted volume fractions of martensite habit plane variants were converted into volume fractions of martensite correspondence variants and their orientation using the Crystallographic Theory of Martensite (CTM) [47] – in particular, Eq. (17) of Ref. [48] was solved. Second, the martensite volume fractions $v_{N\parallel}$ and $v_{N\perp}$ were determined, where $\mathbf{N}$ denotes the plane normal of interest (e.g. [1 0 0] or [0 1 1]) and $\parallel$ and $\perp$ denote whether $\mathbf{N}$ is parallel or perpendicular to the loading axis. Third, the diffracted intensity $I(\mathbf{N})$ of plane $\mathbf{N}$ was normalized by the intensity $I_{ref}(\mathbf{N})$ from a reference test case so that

$$\frac{I(\mathbf{N})}{I_{ref}(\mathbf{N})} \propto \frac{v_N}{v_{N_{ref}}} \tag{1}$$

Load-biased thermal cycling under a bias stress of 100 MPa was chosen as the reference.

3.2. Constitutive relation for austenite–martensite aggregates

The finite element formulation requires a relation between an imposed deformation gradient on an austenite–martensite aggregate and the corresponding increments in average stress, martensite volume fraction and slip system activity. For simulation of entire polycrystals, it is impractical to retain detailed spatial information concerning individual martensite variants; instead, the aggregate is described by the average volume fraction of martensite habit plane variants (plates). The averaging process can be viewed as an isostress approach in that elastic, plastic and transformation processes are driven by a common aggregate Cauchy stress $\mathbf{T}$ and they collectively contribute to the average deformation gradient of the aggregate. These features and improvements to the original formulation [32] are highlighted below.

3.2.1. Partitioning elastic and inelastic deformation

Following Lee [49], the deformation gradient $\mathbf{F} = \mathbf{F}^{e}\,\mathbf{F}^{inel}$, so that it is multiplicatively decomposed into a thermo-elastic part $\mathbf{F}^{e}$ and an inelastic part $\mathbf{F}^{inel}$. Section 3.2.2 describes how $\mathbf{F}^{e}$ is related to the Cauchy stress $\mathbf{T}$ and Sections 3.2.3–5 describe how the time derivative of inelastic deformation $\dot{\mathbf{F}}^{inel}$ is related to $\mathbf{T}$.

3.2.2. Elastic constitutive relation

This section highlights modification of the existing theory to incorporate the full elastic anisotropy of the martensite phase, following Ref. [50]. First, the symmetric Piola–Kirchoff stress $\mathbf{T}^{*}$ and Cauchy stress $\mathbf{T}$ are related by

$$\mathbf{T} = \frac{1}{\det(\mathbf{F}^{e})}\mathbf{F}^{e}\mathbf{T}^{*}\mathbf{F}^{e^{T}} \quad \text{where} \quad \mathbf{T}^{*} = \frac{\partial \boldsymbol{\psi}}{\partial \mathbf{E}^{e}} = \mathbf{C}[\mathbf{E}^{e} - \mathbf{A}_{th}(\theta - \theta_0)] \tag{2}$$

$\boldsymbol{\Psi}_{R}$ denotes the Helmholtz free energy of the austenite–martensite aggregate as defined in Eq. (8) of Ref. [32], and the average elastic strain is $\mathbf{E}^{e} = \tfrac{1}{2}(\mathbf{F}^{eT}\mathbf{F}^{e} - \mathbf{I})$. Eq. (2) requires the aggregate thermal expansion coefficient $\mathbf{A}_{th}$:

$$\mathbf{A}_{th} = v_A\mathbf{A}_{th-A} + v_M\mathbf{A}_{th-M} \tag{3}$$

and effective elastic moduli $\mathbf{C}$:

$$\mathbf{C} = v_A\mathbf{C}_A + \sum_{t=1}^{N_T} v_t\mathbf{C}_{M(t)} \quad \text{where} \quad \mathbf{C}_{M(t)} = v_{t,i}\mathbf{C}_{M(t,i)} + v_{t,j}\mathbf{C}_{M(t,j)} \tag{4}$$

Austenite has cubic symmetry so that $\mathbf{C}_A$ has three independent components. Each habit plate variant t has a local volume fraction v_t and elastic modulus $\mathbf{C}_{M(t)}$, given by the average moduli $\mathbf{C}_{M(t,i)}$, $\mathbf{C}_{M(t,j)}$ and volume fractions $v_{t,i}$, $v_{t,j}$ $(=1 - v_{t,i})$ of the monoclinic (B19′) correspondence variants i and j within plate t. For practical purposes, the components are referred to the austenite crystal basis. This requires the rotation operators $\mathbf{Q}_{t,i}$ and $\mathbf{Q}_{t,j}$ to relate a direction in the martensite crystal basis of variants i and j, respectively, to the crystal basis of austenite from which plate t formed. They are obtained by solving Eq. (17) from the CTM [48]:

$$\mathbf{Q}_{t,i} = \overline{\mathbf{R}}_{ij}\mathbf{R}_{ij}\mathbf{R}_{LC-i} \quad \text{and} \quad \mathbf{Q}_{t,j} = \overline{\mathbf{R}}_{ij}\mathbf{R}_{LC_j} \tag{5}$$

where $\mathbf{R}_{LC\text{-}i}$ and $\mathbf{R}_{LC\text{-}j}$ are the lattice correspondence rotations between martensite variants i and j and austenite, respectively, $\mathbf{R}_{ij}$ is the rotation required to form a twin plane between variants i and j, and $\overline{\mathbf{R}}_{ij}$ is the rotation required to form a habit plane with the austenite [48,50]. Although the thermal expansion coefficient for martensite plates can be constructed in a similar fashion, the isotropic form $\mathbf{A}_{th\text{-}M} = \alpha_M\,\mathbf{I}$ is adopted with the supposition that the primary effect of anisotropy stems from the elastic moduli. This assumption is discussed further in Section 5.2.4 and justified by the small magnitude of thermal strain ($\sim$0.1%) during thermal cycling [37].

3.2.3. Average inelastic velocity gradient for the aggregate

The time derivative of inelastic deformation is $\dot{\mathbf{F}}^{inel} = \mathbf{L}^{inel}\,\mathbf{F}^{inel}$, where the inelastic velocity gradient of the austenite–martensite aggregate is approximated by a rule of mixtures [32]:

$$\mathbf{L}^{inel} = v_A\sum_{s=1}^{N_S}\dot{\gamma}_s\left(\mathbf{b}_s^{slip}\otimes\mathbf{m}_s^{slip}\right) + \sum_{t=1}^{N_T}\dot{v}_t\left(\mathbf{b}_t^{Trans}\otimes\mathbf{m}_t^{Trans}\right); \quad v_A = 1 - v_M \quad \text{and} \quad v_M = \sum_{t=1}^{N_T} v_t \tag{6}$$

The first term is the contribution from plastic deformation of a volume fraction v_A of austenite having N_S slip systems with Burgers vectors $\mathbf{b}_s^{slip}$, slip plane normals $\mathbf{m}_s^{slip}$ and rates $\dot{\gamma}_s$ of slip activities. The second term is the contribution from the rate of increase $\dot{v}_t$ in volume fraction of martensite plate type t (=1–N_T) with habit plane normal $\mathbf{m}_t^{trans}$ and transformation displacement $\mathbf{b}_t^{trans}$. The second equation acknowledges that the austenite plus martensite volume fractions equals 1, and the third equation indicates that the total martensite volume fraction is the sum of the plate volume fractions. $\dot{\gamma}_s$ and $\dot{v}_t$ are related to the Piola–Kirchoff stress $\mathbf{T}^*$ in Sections 3.2.4 and 3.2.5, respectively.

3.2.4. Plastic constitutive relation

The slip rate $\dot{\gamma}_s$ in Eq. (6) is specified according to Peirce et al. [33]:

$$\dot{\gamma}_s = \dot{\gamma}_0 \left|\frac{\tau_s}{g_s}\right|^{(1/m)} \mathrm{sign}(\tau_s); \tau_s = \mathbf{b}_s^{slip} \cdot \left(\mathbf{F}^{e^T}\mathbf{F}^e\mathbf{T}^*\right) \cdot \mathbf{m}_s^{slip} \tag{7}$$

where τ_s is the resolved shear stress on slip system s, $\dot{\gamma}_0$ is a reference shear rate, m is the rate sensitivity and g_s is the slip system hardness that evolves to a saturation value g_{sat} according to

$$\dot{g}_s = \sum_{r=1}^{N_S} h_r(Q + (1-Q)\delta_{sr})|\dot{\gamma}_r| \quad \text{and } h_r = h_0\left(1 - \frac{g_s}{g_{sat}}\right)^a \tag{8}$$

The self and latent hardening rates are h_r and Qh_r, respectively.

3.2.5. Transformation constitutive relation

The rate of change $\dot{v}_t$ is determined by ensuring that the unit volume driving force f_t to form plate type t is bounded as $-f_c \leqslant f_t \leqslant f_c$, where f_c is a critical value and

$$F_t(v_t, \mathbf{T}, \theta) = \mathbf{b}_t^{Trans} \cdot \left(\mathbf{F}^{e^T}\mathbf{F}^e\mathbf{T}^*\right) \cdot \mathbf{m}_t^{Trans} - \frac{\lambda_T}{\theta_T}(\theta - \theta_T) - \sum_{u=1}^{N_T} h_{tu} v_u \tag{9}$$

This formalism, proposed by Thamburaja and Anand [13], specifies no change in v_t when f_t satisfies the inequalities preceding Eq. (9). Should $f_t > f_c$, v_t is increased so as to render $f_t = f_c$ and if $f_t < -f_c$, v_t is decreased so as to render $f_t = f_c$. Thus, it is similar to a plastic yield surface.The driving force f_t has three terms. The first is the mechanical work of the aggregate stress acting through the transformation strain induced by the formation of plate type t. The second is the chemical energy associated with the latent heat of transformation per unit reference volume, λ_T. The third is the interaction between plates in the aggregate. It represents, for example, the additional contribution to f_t due to the stress field of nearby martensite plates u; such detailed interactions are not captured by the aggregate stress in the first term.

4. Calibration of material parameters

Table 1 shows the material parameters used to simulate the 49.9 at.% (55 wt.%) Ni–Ti SMA. They are adopted

Table 1
Calibrated properties for hot rolled/hot drawn polycrystalline 49.9 at.% Ni–Ti (55wt% Ni).

Austenite structure (see Section 3.1.1)		
Property	Value	Calibration feature
Texture	Pole figure (see Fig. 2b)	F1: Fig 2a
Elastic and thermal, $P_{el\text{-}thermal} = \{C_A, C_M, A_{th\text{-}A}, A_{th\text{-}M}\}$ (see Section 4.1)		
$\mathbf{C}_A$ (GPa)	$C_{11} = 183$ $C_{12} = 146$ $C_{44} = 46$	F2: DFT calculations [34]
$\mathbf{C}_M$ (GPa)	$C_{11} = 249$ $C_{12} = 129$ $C_{13} = 107$ $C_{15} = 15$ $C_{22} = 245$ $C_{23} = 125$ $C_{25} = -3$ $C_{33} = 212$ $C_{35} = -1$ $C_{44} = 87$ $C_{46} = -4$ $C_{55} = 66$ $C_{66} = 86$ Hill Averages: $E = 180$, $G = 69$	F2: DFT calculations [34]
α_A (K^{-1})	11×10^{-6}	F3: Neutron diffraction [37]
α_M (K^{-1})	6.6×10^{-6}	F4: Neutron diffraction [37]
Phase transformation, $P_{trans} = \{\theta_T, \lambda_T, f_c \text{ and } h_{tu}\}$ (see Section 4.2)		
θ_T (K)	353.7	F5: DSC data
λ_T (MJ m^{-3})	140 initial guess: 165.6	F11–13: Fig. 3a F5: DSC data
f_c (MPa)	$0.051\lambda_T$ (=7.14)	F6: Fig. 1a and Eq. (10):
h_{tu} (MPa)	$h_{com} = 0$; $h_{inc} = C_{A(44)}/12{,}000$; $h_{self} = C_{A(44)}/400$	F7–8: Fig. 1a. F9: Fig. 3a and (11) See also Table 2 [15]
Austenite plasticity, $P_{plastic} = \{\dot{\gamma}_0, g_{sat}, g_s^0, h_0, Q, a, E_{p(pre)}\}$ (see Section 4.3)		
$\dot{\gamma}_0$ (s^{-1})	0.002	F10: literature [32]
m	0.02	F10: literature [32]
Q	1.4	F10: literature [32]
a	0.125	F10: literature [32]
g_{sat} (MPa)	900	F10: literature [32]
g_s^0 (MPa)	272	F11–14: Fig. 3a
h_0 (MPa)	50	F11–14: Fig. 3a
$E_{p(pre)}$ (%)	−0.7	F11–14: Fig. 3a

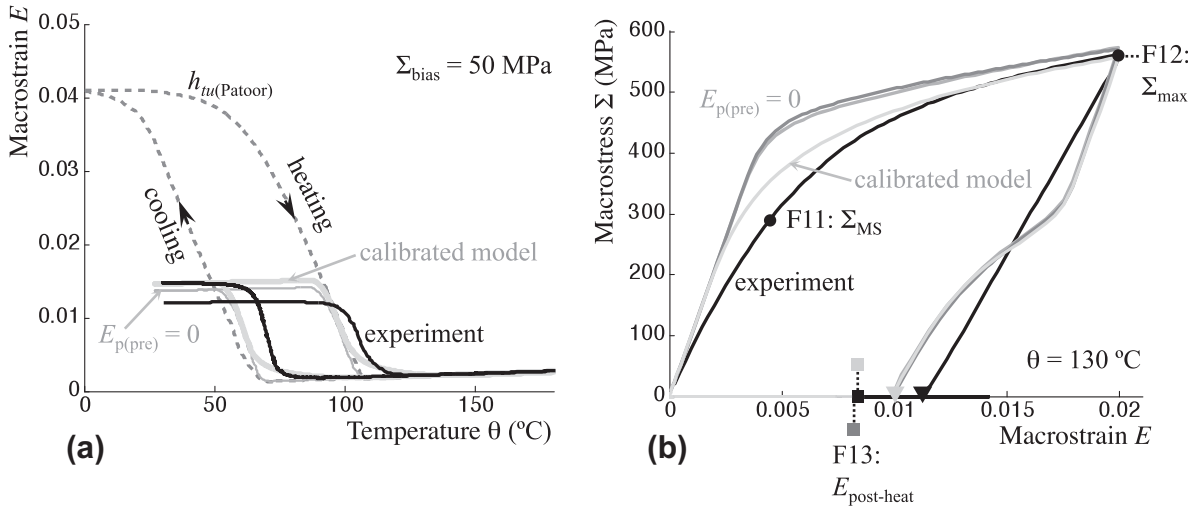

Fig. 4. (a) Axial macrostrain E vs. temperature θ during thermal cycling with an axial bias stress $\Sigma_{bias} = 50$ MPa and (b) axial macrostress Σ vs. macrostrain E at $\theta_0 = 130$ °C for the polycrystalline 49.9 at.% Ni–Ti alloy. The calibrated model parameters are in Table 1. Other results in (a) use the calibrated parameters except with the interaction matrix h_{tu} of Patoor et al. [23] or with $E_{p(pre)} = 0$. The $E_{p(pre)} = 0$ cases in (b) are nearly coincident and use $(g_s^0, h_0) = (235$ MPa, 500 MPa) vs. (250 MPa, 50 MPa) (the former is slightly higher).

from published literature values or calibrated to DSC data and select isothermal deformation and thermal cycling tests performed specifically to support this modeling effort. These various "features" and the calibration process are described in Sections 4.1–4.3.

4.1. Elastic-thermal, $P_{el\text{-}thermal} = \{C_A,\ C_M,\ A_{th\text{-}A},\ A_{th\text{-}M}\}$

The anisotropic elastic stiffness $\mathbf{C}_A$ for the cubic (B2) austenite phase and $\mathbf{C}_M$ for the monoclinic (B19′) martensite phase are adopted from the density functional theory calculations (feature **F2**, Table 1) of Hatcher et al. [34]. Isotropic thermal expansion properties are assumed with α_A and α_M taken from the neutron diffraction experiments (feature **F3**, Table 1) of Qiu et al. [37]. Use of recently computed elastic moduli corrects frequent assumptions in the literature that $\mathbf{C}_M \sim \frac{1}{2}\mathbf{C}_A$ (e.g. [12,13]) or $\mathbf{C}_M \leqslant \mathbf{C}_A$ (e.g. [7,9,15–18]. These effects, including differences in moduli from Hatcher et al. [34] vs. Wagner et al. [51], are discussed in Section 5.2.4.

4.2. Transformation, $P_{trans} = \{\theta_T,\ \lambda_T,\ f_c$ and $h_{tu}\}$

This study models $N_T = 24$ type-II twinned martensite plate types, like many micromechanics-based models [13,15–17,26], although there are 192 theoretically possible habit plane variants (hpv) for B2 → B19′ transformation [47]. The transformation parameters P_{trans} are obtained from a combination of DSC (no load), isothermal deformation tests and thermal cycling data at $\Sigma_{bias} = 50$ MPa. The DSC data (averaged over seven samples) gives θ_{MF}, θ_{MS}, θ_{AS} and $\theta_{AF} = 46$, 71, 86 and 109 ± 2 °C, respectively, for this 49 at.% Ni–Ti alloy. These values (feature **F4**) furnish the transformation temperature $\theta_T = (\theta_{MS} + \theta_{AS})/2 = 353.7$ K (standard deviation = 2 K). The calibrated simulations use a latent heat of transformation $\lambda_T = 140$ MJ m^{-3}, as detailed in Section 4.3. Initially, an average of Q_{DSC} (feature **F5**) for the forward A → M and reverse M → A heats of transformation is used, yielding $\lambda_T \approx Q_{DSC} = 165.6$ MJ m^{-3} (standard deviation = 4.7 MJ m^{-3}). This is viewed as an initial guess since Q_{DSC} includes contributions from elastic or defect energies associated with the transformation.

The critical driving force for transformation is obtained from

$$\frac{f_c}{\lambda_T} = \frac{\theta^{M\to A} - \theta^{A\to M}}{2\theta_T} = \frac{\Delta\theta_H}{2\theta_T} \tag{10}$$

Eq. (10) is obtained by writing the forward ($f_t^{A\to M} = f_c$) and backward ($f_t^{M\to A} = -f_c$) critical conditions in extended form using Eq. (9) and then taking the difference between them. Eq. (10) furnishes $f_c/\lambda_T = 0.051$, based on an average hysteretic width (feature **F6**) $\Delta\theta_H = 36.3$ K (standard deviation = 1.15 K) for thermal cycling at $\Sigma_{bias} = 50$ MPa (see Fig. 1a). This small Σ_{bias} minimizes plasticity; a similar f_c/λ_T value occurs with $\Sigma_{bias} = 0$ data. Formally, $\Delta\theta_H$ is an average width over the range $\xi = 0.1$–0.9, where ξ is the fraction of transformation strain.

The structure of the martensite plate interaction matrix h_{tu} in Eq. (9) is obtained by calibrating the simulations to give $E_T \approx 1\%$ (feature **F7**) and $\Delta\theta^{A\to M} \approx 25$ °C (feature **F8**) at $\Sigma_{bias} = 50$ MPa. $\Delta\theta^{A\to M}$ is the decrease ($\theta_{MF} - \theta_{MS}$) in temperature to complete the A → M transformation. The outcome is that h_{tu} must have three independent values:

$$h_{tu} = \begin{cases} h_{self} (= C_{A(44)}/400) & \text{if } t = u \\ h_{com} (= 0) & \text{if } t \neq u \text{ and } \det(\epsilon_{T(t)} - \epsilon_{T(u)}) = 0 \\ h_{in} (= C_{A(44)}/12000) & \text{if } t \neq u \text{ and } \det(\epsilon_{T(t)} - \epsilon_{T(u)}) \neq 0 \end{cases} \tag{11}$$

This structure is a modification to the popular form proposed by Patoor et al. [23], where $h_{self} = h_{com} =$

$C_{A(44)}$/3000 MPa and $h_{inc} = C_{A(44)}$/750 MPa are used for NiTi [15–17]. The rationale for the modification is that simulations employing the Patoor et al. [23] structure (curve $h_{tu(Patoor)}$, Fig. 4a) give $E_T \sim 4\%$ for $\Sigma_{bias} = 50$ MPa, and thus over-predict the experimental values, regardless of the assumed $C_{A(44)}$ value. Martensite plates with maximal transformation strain along the loading axis dominate over other plate types because the stress work (term 1 in f_t, Eq. (9)) initially renders the driving force f_+ largest for this favored (+) plate type. As long as $h_{com} < h_{inc}$, the favored (+) plates experience less hardening than non-favored (–) plates, because $-\partial f_+/\partial v_+ < \partial f_-/\partial v_+$. The modification sets $h_{self} \gg h_{com}, h_{inc}$ to suppress formation of a single plate type.

The calibration is guided by application of Eq. (9) to an idealized case of two populations of plate types: a favored (+) type that renders a transformation strain $E_{T(max)}$ if $v_+ \to 1$ and a non-favored (–) collection of self-accommodating plate types that renders $E_T \sim 0$ if $v_- \to 1$. Taking the difference between the critical force conditions $f_+ = f_c$ and $f_- = f_c$ furnishes

$$S_+ \underset{bias}{\Sigma} = \frac{\Delta h_{+-}}{2}\left(\frac{\sigma_T}{\sigma_T^{max}} + 1\right) + \frac{\Delta h_{-+}}{2}\left(\frac{\sigma_T}{\sigma_T^{max}} - 1\right) \tag{12}$$

where $S_+\Sigma_{bias}$ is the aggregate stress work to form favored plates and $\Delta h_{+-} = h_{++} - h_{-+}$ and $\Delta h_{-+} = h_{--} - h_{+-}$ are differences in interaction elements. Thus, increases in the differences (h_{self}–h_{com}) and (h_{self}–h_{inc}) increase the required $S_+\Sigma_{bias}$ for favored plates, decreasing E_T. Eq. (9) also furnishes

$$\lambda_T \frac{\theta_{MS} - \theta_{MF}}{\theta_T} = \frac{\Delta h_{++}}{\Delta h_{+-} + \Delta h_{-+}}(S_+ \underset{bias}{\Sigma} + \Delta h_{-+}) + h_{+-} \quad \text{and}$$

$$\underset{max}{\Sigma} - \underset{MS}{\Sigma} \approx \frac{h_{self}}{S_+} \tag{13}$$

where $h_{++} = h_{++} - h_{+-}$. The second equation of Eqs. (13) suggests that h_{self} can be determined from the difference, $\Sigma_{max} - \Sigma_{MS}$ (feature **F9**), from isothermal deformation tests (Fig. 3a). Further, Eq. (12) and the first equation of Eqs. (13) suggest that differences such as $h_{self} - h_{com}$ and $h_{self} - h_{inc}$ can be determined by capturing Features **F7** and **F8** for thermal cycling at low bias stress (Fig. 1a). The final results reported in Eq. (11) and Table 1 are obtained as a best fit.

4.3. Austenite plasticity, $P_{plastic} = \{\dot{\gamma}_0, m, g_s^0, g_{sat}, h_0, Q, a, E_{p(pre)}\}$ and λ_T update

These parameters are obtained from literature values and additional isothermal deformation data. In particular, 6 {1 1 0}/⟨1 0 0⟩ and 6 {0 0 1}/⟨1 0 0⟩ austenitic slip systems are considered [52]. The rate sensitivity $m = 0.02$, reference strain rate $\dot{\gamma}_0 = 10^{-3}\ s^{-1}$ ($\dot{E} \geqslant 10^{-4}\ s^{-1}$), $Q = 1.4$, $a = 0.125$ and $g_{sat} = 900$ MPa (see Eqs. (7) and (8)) are adopted from prior calibration of the model to single crystal pseudoelastic compression tests (feature **F10**), using loading orientations that enhance plasticity [32]. In reality, there is limited data to determine these parameters accurately, but the simulations are less sensitive to them. The remaining plasticity parameters are the threshold resolved shear stress g_s^0 for plastic flow, initial strain hardening h_0 and plastic pre-deformation $E_{p(pre)}$. The resulting calibration gives a best fit of $g_s^0 = 272$ MPa, $h_0 = 50$ MPa, $E_{p(pre)} = -0.7\%$ and $\lambda_T = 140\ MJ\ m^{-3}$ (updated from an initial guess 165.6 MJ m^{-3}).

More specifically, the calibration procedure matches Σ_{MS}, Σ_{max} and $E_{post\text{-}heat} = 0.0085$ for $E_{max} = 0.02$ (Features **F11–13**, Fig. 4b). The updated, smaller λ_T decreases Σ_{MS} and Σ_{max} to better match the data, but g_s^0 and h_0 are indeterminant. For example, the same curve ($E_{p(pre)} = 0$, Fig. 4b) is obtained for (g_s^0, h_0) = (250 MPa, 50 MPa) vs. (235 MPa, 500 MPa). The first case is selected since it better matches $E_{post\text{-}heat} = 0.0204$ (feature **F14**, Fig. 3a). The second case under predicts the value.

A final issue is that curve $E_{p(pre)} = 0$ (Fig. 4b) over predicts Σ_{MS} (feature **F11**). Prior work [32] demonstrates that compressive prestraining decreases Σ_{MS} and increases hardening. The "calibrated model" result (Fig. 4b) adopts $E_{p(pre)} = -0.7\%$ and (g_s^0, h_0) = (272 MPa, 50 MPa) as a best match. A larger compressive prestrain does not improve the match. This pre-deformation produces a multi-axial and spatially varying residual stress distribution with stress in the loading direction varying from −345 MPa to 272 MPa. These magnitudes are a substantial fraction of Σ_{MS} (feature **F11**) in Fig. 3a.

5. Model assessment

5.1. Isothermal deformation response

The calibrated model captures the monotonic loading paths for different E_{max} and θ. In particular, Σ_{max} for $\theta = 130$ °C (Pt A, Fig. 3b) agrees with experiments. Also, both experiments and simulations show an upward shift $\Delta\Sigma \sim 100$ MPa when θ increases to 215 °C (Fig. 3b). If plasticity is "turned off" in the simulations, an excessive shift $\Delta\Sigma = 627$ MPa occurs. This is consistent with a Clausius–Clapeyron slope $d\Sigma/d\theta = 6.2\ MPa\ K^{-1}$ for favorably oriented martensite plates [15,53]. The simulations show that plasticity intervenes to lower the shift; it is driven by complex, multi-axial stress states inherent in polycrystals.

The discrepancy between the experimental and simulated unloading paths suggests that the reverse (M → A) transformation is complex. The experimental unloading paths are relatively linear (Fig. 3a), with most of the stress-induced martensite recovered during subsequent heating rather than during unloading. The simulated unloading path ($\theta = 130$ °C, Fig. 3b) is the opposite, with most of the stress-induced martensite recovered during unloading rather than heating. A possible interpretation is that the simulations underestimate f_c for the reverse transformation. This might be due to coupling between

plasticity and transformation at fine (variant) scales – a phenomenon not captured explicitly by the aggregate formulation.

5.2. Thermal cycling response

Overall, several experimental trends are captured, including the textured nature of martensite, but again there are quantitative discrepancies.

5.2.1. Effect of bias stress and prestrain on transformation strain and critical temperatures

Consistent with experiments, the predicted transformation strain E_T increases with Σ_{bias}, as do the critical temperatures θ_{AS}, θ_{AF}, θ_{MS} and θ_{MF}, and the temperature difference $\theta_{MS} - \theta_{MF}$ (Fig. 1). Fig. 5 shows that even the two-way response for thermal cycling at $\Sigma_{bias} = 0$ is captured. This demonstrates that a plastic predeformation $E_{p(pre)} = -0.7\%$ creates a positive E_T, by inducing an internal stress state that biases martensite plate formation. Conversely, a negative E_T is generated for $E_{p(pre)} > 0$. It is interesting that a nonzero E_T occurs, even though the average internal stress is zero.

Fig. 6 shows that the simulations capture a peak in E_T with Σ_{bias}. This is due primarily to the new proposed structure for h_{tu} (Eq. (11)) and the coupling of crystal plasticity and transformation (Eq. (6)). These features cause E_T to increase gradually with Σ_{bias} due to formation of the favored (+) martensite. For $\Sigma_{bias} > 350$ MPa, the model predicts a decrease in E_T with Σ_{bias} due to the onset of open loop strain, ΔE_{cycle} (see Fig. 8). The predicted effect of $E_{p(pre)} = -0.7\%$ vs. 0 on the E_T–Σ_{bias} response in Fig. 6 is negligible. For comparison, simulations using the Patoor et al. [23] structure for h_{tu} substantially overestimate E_T at small Σ_{bias} (curve $h_{tu(Patoor)}$, Fig. 6) and predict E_T to be relatively independent of Σ_{bias}, contrary to these and previous experimental results [1–3,30].

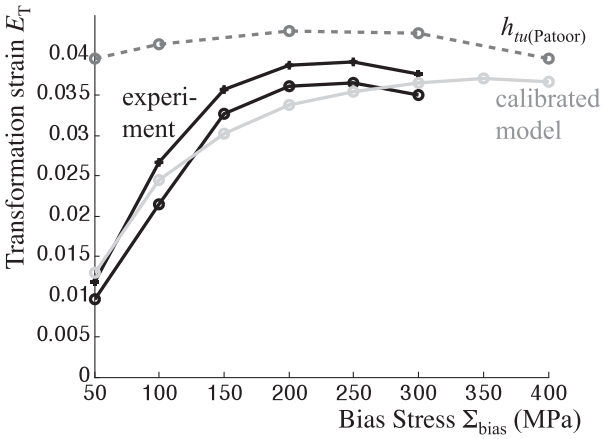

Fig. 6. Axial transformation strain E_T vs. bias stress Σ_{bias} during thermal cycling between $\theta_{min} = 30$ °C and $\theta_{max} = 165$ °C (lower experimental curve) vs. 200 °C (upper experimental curve) for the polycrystalline 49.9 at.% Ni–Ti alloy. The calibrated model parameters are presented in Table 1. Also shown is the calibrated model result using the interaction matrix h_{tu} of Patoor et al. [23]. The model results are insensitive to $\theta_{max} = 165$ vs. 200 °C.

5.2.2. Plastic strain enhancement due to phase transformation

Simulations of thermal cycling at large Σ_{bias} (400 MPa) reveal that transformation enhances the macroscopic plastic strain E_p. Fig. 7 shows rather modest increases in E_p with thermal cycling for the "plasticity only" case – where transformation is turned off. In contrast, E_p is larger in the "calibrated model" case, where both transformation and plasticity are present. The largest increases in E_p occur during the early stages of cooling and latter stages of heating, when v_M is small (see regions 1 and 2, Fig. 7). The phenomenon is reminiscent of ratcheting of E_p during stress-biased thermal cycling of composites with a large thermal strain mismatch between constituents [54]. These predictions are consistent with prior work [32] showing that plasticity aids

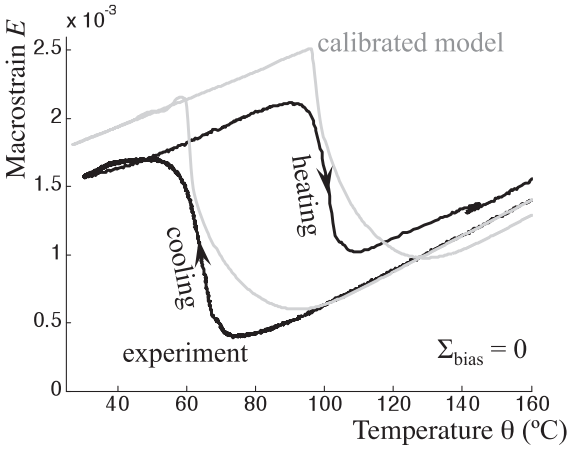

Fig. 5. Axial macrostrain E vs. temperature θ during no-load thermal cycling of the polycrystalline 49.9 at.% Ni–Ti alloy, showing a two-way effect. The calibrated model parameters are presented in Table 1.

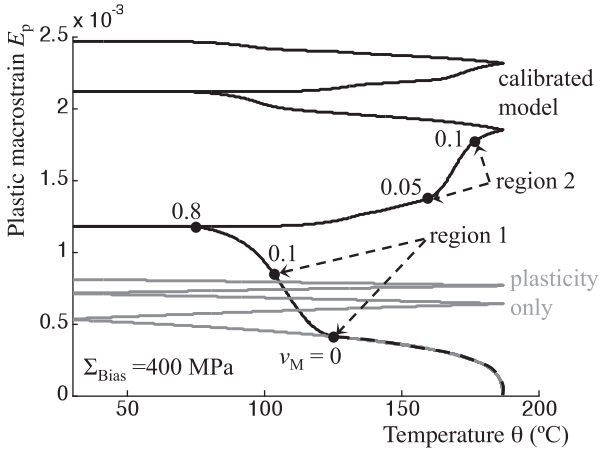

Fig. 7. Predicted axial plastic macrostrain E_p vs. temperature θ during thermal cycling with an axial bias stress $\Sigma_{bias} = 400$ MPa. The calibrated model parameters are presented in Table 1. The "plasticity only" case uses the calibrated model without any phase transformations.

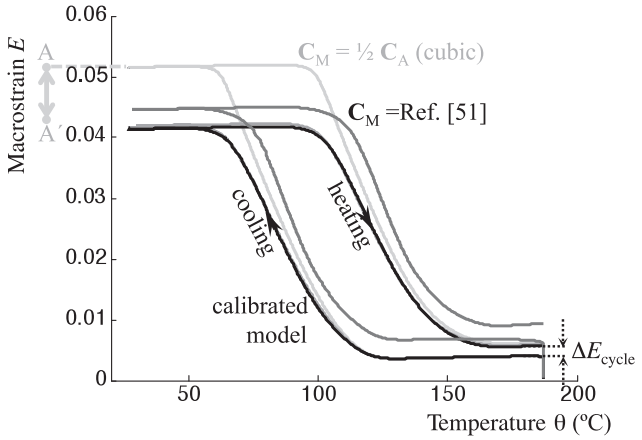

Fig. 8. Axial macrostrain E vs. temperature θ during thermal cycling with an axial bias stress $\Sigma_{bias} = 400$ MPa, showing predictions of the calibrated model, which uses elastic constants $\mathbf{C}_M$ and $\mathbf{C}_A$ from Ref. [34]. Also shown are the calibrated model predictions with $\mathbf{C}_M \sim \frac{1}{2}\,\mathbf{C}_A$, $\mathbf{C}_M$ and $\mathbf{C}_A$ from Ref. [51], and $\mathbf{C}_M = \mathbf{C}_{M(Isotropic)}$. The last uses an isotropic matrix with Young's modulus E and elastic shear modulus G given by the Hill averages (Table 1). It overlaps the original calibrated model result.

martensite transformation during pseudoelastic loading to some macroscopic stress $\boldsymbol{\Sigma}$.

5.2.3. Discrepancy in open loop strain

An important quantitative discrepancy is the underestimate of incremental strain per thermal cycle, ΔE_{cycle}, or "open loop strain" (Fig. 1). Although transformation is predicted to enhance plasticity, the simulations predict noticeable ΔE_{cycle} values only at large Σ_{bias} (>350 MPa) while experiments show noticeable values even at small Σ_{bias} (50 MPa). This discrepancy may be due to the nature of the "aggregate" constitutive relation (Section 3.2.3) and the assumption that the rate of slip activity ($\dot{\gamma}_s$, Section 3.2.4) and rate of martensite formation ($\dot{v}_t$, Section 3.2.5) are both computed from the average aggregate stress. In reality, the local stress field around martensite plates can be sufficiently large to drive local plasticity, as evidenced by recent transmission electron microscopy of dislocation content in micron-scale, pseudoelastically compressed single crystals [27] and load-biased thermal cycling of larger single crystals [30].

5.2.4. Assumptions concerning martensite elastic moduli and thermal expansion coefficients

The simulations reveal several aspects concerning elastic moduli and thermal expansion coefficients. First, Fig. 8 shows that the predicted transformation strain E_T during thermal cycling is about 0.01 greater if a common assumption, $\mathbf{C}_M \sim \frac{1}{2}\,\mathbf{C}_A$, is used (e.g. [12,13]). This assumption is erroneous since both experiments [55,56] and first principle calculations [34,51] show that martensite is stiffer than austenite (Table 1). A more compliant martensite increases E_T by increasing the elastic strain and texturing in the martensite; the former is deduced from the unloading path from A to A' in Fig. 8. A reasonable approximation to the calibrated results is to use $\mathbf{C}_M = \mathbf{C}_{M(isotropic)}$, where $\mathbf{C}_{M(isotropic)}$ is an isotropic matrix with Young's and shear moduli given by Hill's averages (see Table 1). The results are based on the anisotropic moduli of Hatcher et al. [34]. If values from Wagner and Windl [51] are used, smaller Hill's averages result ($E_h = 122$ GPa, $G_h = 45$ GPa), but $\mathbf{C}_A$ is also smaller. The net effect is a ~0.3% increase in E_T (Fig. 8), i.e. it is virtually unchanged. The observation that martensite can be represented by average isotropic elastic moduli suggests that it is also reasonable to use isotropic thermal expansion coefficients, at least for aggregate-scale simulations. This supports the adoption of isotropic descriptions for $\mathbf{A}_{th\text{-}A}$ and $\mathbf{A}_{th\text{-}M}$ in Section 4.1.

5.2.5. Texture evolution

The calibrated simulations are qualitatively consistent with measurements of textured martensite formation

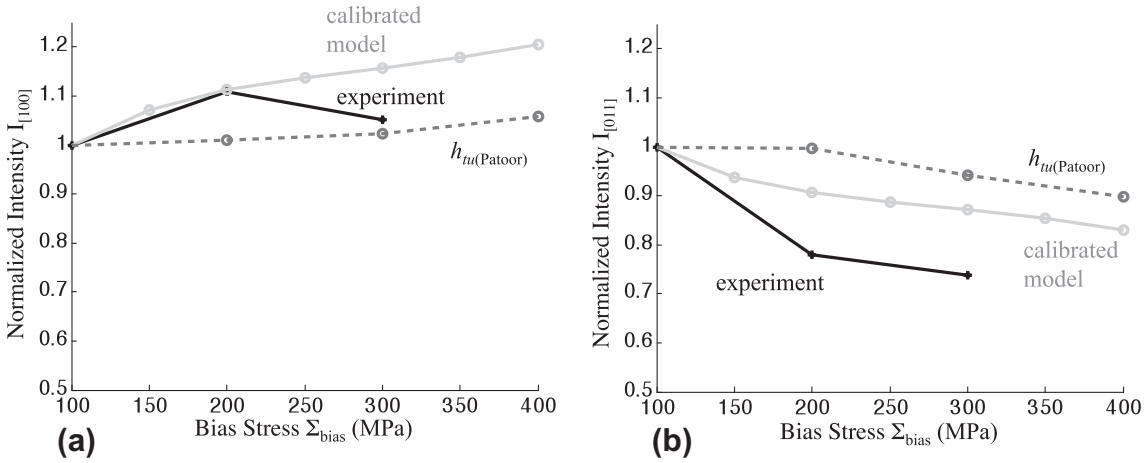

Fig. 9. Normalized neutron diffraction intensities I vs. bias stress Σ_{bias} for (a) (1 0 0) and (b) (0 1 1) martensite planes oriented parallel to the loading axis, for the 49.9 at.% Ni–Ti alloy. The intensities are measured at $\theta_{min} = 30$ °C, following thermal cycling to $\theta_{max} = 230$ °C, and are normalized by the intensity at $\Sigma_{bias} = 100$ MPa. The experimental data is from Ref. [2]. The calibrated model parameters are presented in Table 1. Also shown is the calibrated model result using the interaction matrix h_{tu} of Patoor et al. [23].

during thermal cycling at $\Sigma_{bias} = -150$ MPa. During heating to 130 °C, in situ neutron diffraction reveals peaks from retained martensite with plane normals $\mathbf{N} = [0\ 1\ 1] \perp$ to the loading axis and also $\mathbf{N} = [1\ 0\ 0] \parallel$ to the loading axis. Martensite with $\mathbf{N} = [0\ 1\ 1] \parallel$ or $\mathbf{N} = [1\ 0\ 0] \perp$ is not observed [56]. The calibrated model predicts the same results at 130 °C; in particular, there is 5% retained martensite, some of which has $\mathbf{N} = [0\ 1\ 1] \perp$ and $\mathbf{N} = [1\ 0\ 0] \parallel$, but none has $\mathbf{N} = [0\ 1\ 1] \parallel$ or $\mathbf{N} = [1\ 0\ 0] \perp$. This complements earlier work by Gao et al. [57], where isothermal loading was considered instead of thermal cycling.

Fig. 9 shows that the calibrated model qualitatively captures the relative trends in $[1\ 0\ 0] \parallel$ and $[0\ 1\ 1] \parallel$ intensities with increasing Σ_{bias}. The intensities are measured at $\theta_{min} = 30$ °C and are normalized by values at $\Sigma_{bias} = 100$ MPa. The simulation results depend slightly on $E_{p(pre)}$ because the residual stress state aids or opposes the bias stress, depending on the location. For example, the normalized intensity $[1\ 0\ 0]$ shifts downward by ~0.03 for $E_{p(pre)} = 0$ (vs. −0.7%) and $[0\ 1\ 1]$ is unchanged. Results using the hardening matrix of Patoor et al. [23] (see the discussion following Eq. (11)) tend to be less dependent on Σ_{bias} because the martensite texture is over-predicted at small Σ_{bias}, leaving little room for additional texturing at larger Σ_{bias}.

6. Conclusions

Several key elements are required to capture the thermal cycling and isothermal deformation trends for polycrystalline NiTi (49.9 at.% Ni). A critical feature is the coupling of transformation and plasticity. With appropriate data, the calibrated model captures (i) the effect of temperature on isothermal deformation loading response; (ii) the effect of bias stress on critical temperatures, transformation strain and martensite texture evolution during thermal cycling; and (iii) the effect of deformation processing in the austenitic state on the two-way effect and uniaxial loading at $\theta > \theta_{AF}$.

Two other key elements are the incorporation of anisotropic elasticity and an augmented form of the martensite hardening matrix h_{tu} (Eq. (11)). The first corrects a frequent assumption that martensite moduli are ~½ those of austenite. The augmented h_{tu} (Eq. (11)) increases the self-hardening term, thereby capturing the gradual increase in transformation strain and martensite texture with bias stress during thermal cycling.

The simulations capture plasticity–transformation coupling in an aggregate sense but not on the martensite plate scale. On this smaller scale, retained martensite can affect texture evolution, and the stress redistribution in the vicinity of the plates may promote dislocation substructure [27–30] and affect the critical driving force for martensite formation (f_c, Eq. (9)). Some consequences are discrepancies in the amount of reverse transformation during unloading and subsequent heat treatment (Fig. 3), the magnitude of ratcheting during thermal cycling under a bias stress (Fig. 1), and the effect of upper cycle temperature on transformation strain (Fig. 6) [2]. In principle, the use of 24 type II rather than all 192 predicted type I and type II habit plane variants [48] may affect martensite texture predictions, but it is unlikely to address the aforementioned discrepancies.

Concerning future activities, the present work could benefit, in principle, from detailed studies of variant–variant and variant–plasticity interaction within aggregates. For example, the recursive method of Sittner and Novak [21,22] provides a modeling-experiment approach with which to supplant the martensite hardening matrix (h_{tu}) in the present FE simulations. However, the present work also requires information about phase transformation–plasticity coupling at the subaggregate (discrete variant) scale. Currently, quantitative information about such coupling is lacking. Inelastic deformation processes in martensite, such as detwinning and reorientation, can be addressed as described by Pan et al. [26]. In principle, martensite plasticity can also be incorporated, but detailed experimental evidence of operative slip systems and critical stresses for activation is lacking. Given the recent observations of complex dislocation structures induced by transformation [25,29,30], it is remarkable that an aggregate-based, grain-scale model is so successful.

Acknowledgements

D.G. and R.N. acknowledge support from the NASA Fundamental Aeronautics Program (Dr. Dale Hopkins, API). P.M.A. and S.M. acknowledge Dr. Myoung-Gyu Lee (assistance with texture analysis), Dr. Michael Mills (discussions about austenite plasticity), Dr. Nick Hatcher (elastic constants), the NASA Fundamental Aeronautics Program, Supersonics Project (Grant No. NNX08AB49A), the Department of Energy (Grant No. DE-SC0001258) and the Ohio Supercomputer Center (Grant No. PAS676). R.V. and O.B. acknowledge experimental assistance from Sven Vogel at Los Alamos National Laboratory, the NASA Fundamental Aeronautics Program, Supersonics Project (Grant No. NNX08AB51A) and the Florida Center for Advanced Aeropropulsion.

References

[1] Wu XD, Sun GJ, Wu JS. Mater Lett 2003;57:1334.
[2] Padula SA, Qiu S, Gaydosh DJ, Noebe RD, Bigelow GS, Garg A, Vaidyanathan R. Metall Mater Trans A 2011; accepted for publication.
[3] Padula SA, Gaydosh DJ, Noebe RD, Bigelow GS, Garg A, Lagoudas D, et al. In: Dapino MJ, Ounaies Z, editors, Behavior and mechanics of multifunctional and composite materials, vol. 6929. Bellingham: Spie-Int Soc Optical Engineering; 2008. p. 92912.
[4] Grossman CH, Frenzel J, Sampath V, Depka T, Eggeler G. Metall Mater Trans A 2009;40A:2530.
[5] Bekker A, Brinson LC. J Mech Phys Solids 1997;45:949.
[6] Panico M, Brinson LC. J Mech Phys Solids 2007;55:2491.
[7] Boyd JG, Lagoudas DC. Int J Plasticity 1996;12:805.
[8] Hartl DJ, Chatzigeorgiou G, Lagoudas DC. Int J Plasticity 2010;10:1485.
[9] Lagoudas DC, Entchev PB. Mech Mater 2004;36:865.

[10] Lagoudas DC, Entchev PB, Popov P, Patoor E, Brinson LC, Gao XJ. Mech Mater 2006;38:430.
[11] Patoor E, Lagoudas DC, Entchev PB, Brinson LC, Gao XJ. Mech Mater 2006;38:391.
[12] Anand L, Gurtin ME. J Mech Phys Solids 2003;51:1015.
[13] Thamburaja P, Anand L. Int J Plasticity 2002;18:1607.
[14] Siredey N, Patoor E, Berveiller M, Eberhardt A. Int J Solids Struct 1999;36:4289.
[15] Gall K, Sehitoglu H. Int J Plasticity 1999;15:69.
[16] Lim TJ, McDowell DL. J Mech Phys Solids 2002;50:651.
[17] Wang XM, Xu BX, Yue ZF. Int J Plasticity 2008;24:1307.
[18] Kouznetsova VG, Geers MGD. Mech Mater 2008;40:641.
[19] Idesman AV, Cho JY, Levitas VI. Appl Phys Lett 2008:93.
[20] Hackl K, Heinen R, Schmahl W, Hasan H. Mater Sci Eng A 2007;347:481–2.
[21] Novák V, Sittner P. Mater Sci Eng A 2004;378:490.
[22] Sittner P, Novák V. Scripta Mater 2004;51:321.
[23] Patoor E, Eberhardt A, Berveiller M. J Phys IV 1996;6:277.
[24] Gao XJ, Huang MS, Brinson LC. Int J Plasticity 2000;16:1345.
[25] Niclaeys C, Ben Zineb T, Arbab-Chirani S, Patoor E. Int J Plasticity 2002;18:1619.
[26] Pan H, Thamburaja P, Chau FS. Int J Plasticity 2007;23:711.
[27] Norfleet DM, Sarosi PM, Manchiraju S, Wagner MFX, Uchic MD, Anderson PM, et al. Acta Mater 2009;57:3549.
[28] Delville R, Malard B, Pilch J, Sittner P, Schryvers D. Int J Plasticity 2011;27:282.
[29] Simon T, Kroger A, Somsen C, Dlouhy A, Eggeler G. Acta Mater 2010;58:1850.
[30] Hamilton RF, Sehitoglu H, Chumlyakov Y, Maier HJ. Acta Mater 2004;52:3383.
[31] Jones NG, Dye D. Intermetallics, doi:10.1016/j.intermet.2011.03.032.
[32] Manchiraju S, Anderson PM. Int J Plasticity 2010;10:1508.
[33] Peirce D, Asaro RJ, Needleman A. Acta Metall 1982;30:1087.
[34] Hatcher N, Kontsevoi OY, Freeman AJ. Phys Rev B 2009:80.
[35] Heinen R, Hackl K, Windl W, Wagner MFX. Acta Mater 2009;57:3856.
[36] Wenk HR, Lutterotti L, Vogel S. Nucl Instrum Meth Phys Res Sec A 2003;515:575.
[37] Qiu S, Krishnan VB, Padula SA, Noebe RD, Brown DW, Clausen B, et al. Appl Phys Lett 2009:95.
[38] Jiang F, Liu Y, Yang H, Li L, Zheng Y. Acta Mater 2009;57:4773.
[39] Bigalow GS, Garg A, Padula SA, Gaydosh DJ, Noebe RD. Scripta Mater 2011;64:725.
[40] Gall K, Maier HJ. Acta Mater 2002;50:4643.
[41] Frick CP, Ortega AM, Tyber J, Maksound AEM, Maier HJ, Liu Y, et al. Mater Sci Eng A 2005;405:34.
[42] Olgricht J, Yawny A, Condo AM, Lovey FC, Eggeler G. Mater Sci Eng A 2008;142:481–2.
[43] Miyazaki S, Ohmi Y, Otsuka K, Suzuki Y. J Phys 1982; 43(Suppl 120):C4–255.
[44] Otsuka K, Ren Z. Prog Mater Sci 2005;50:511.
[45] ABAQUS reference manuals, Providence, RI; 2008.
[46] Kallend JKU, Rollett S, Wenk H. The preferred orientation package from Los Alamos, Los Alamos National Laboratory. Warrendale, PA: TMS; 1989.
[47] Bhattacharya K. Microstructure of martensite. Oxford: Oxford University Press; 2003.
[48] Hane KF, Shield TW. Acta Mater 1999;47:2603.
[49] Lee EH. J Appl Mech 1969;36:1.
[50] Turteltaub S, Suiker ASJ. Int J Solids Struct 2006;43:4509.
[51] Wagner MFX, Windl W. Acta Mater 2008;56:6232.
[52] Chumlyakov YI, Surikova NS, Korotayev AD. Fizika Metallov I Metallovedenie 1996;82:148.
[53] McKelvey AL, Ritchie RO. Philos Mag A 2000;80:1759.
[54] Zhang HY, Anderson PM, Daehn GS. Metall Mater Trans A 1994;25:415.
[55] Rajagopalan S, Little AL, Bourke MAM, Vaidyanathan R. Appl Phys Lett 2005;86:3.
[56] Qiu S, Padula SA, Noebe RD, Gaydosh DJ, Vaidyanathan R. Acta Mater 2011;59:5055–66.
[57] Gao XJ, Brown DW, Brinson LC. Smart Struct Integ Sys 2005;5764:715.